Effects of uniaxial and shear strains on the electronic spectrum of Lieb and kagome lattices

W. P. Lima,[1,*] D. R. da Costa,[1,2,†] S. H. R. Sena,[3,‡] and J. Milton Pereira, Jr.[1,§]

[1]*Departamento de Física, Universidade Federal do Ceará, Campus do Pici, 60455-900 Fortaleza, Ceará, Brazil*

[2]*Key Laboratory for Micro/Nano Optoelectronic Devices of Ministry of Education & Hunan Provincial Key Laboratory of Low-Dimensional Structural Physics and Devices, School of Physics and Electronics, Hunan University, Changsha 410082, China*

[3]*Instituto de Ciências Exatas e da Natureza, Universidade da Integração Internacional da Lusofonia Afro-Brasileira, Campus das Auroras, 62790-970 Redenção, Ceará, Brazil*

(Received 18 January 2023; revised 15 August 2023; accepted 11 September 2023; published 26 September 2023)

We systematically study the effects of the shear and uniaxial strains, applied along different crystallographic directions, on the electronic spectrum of Lieb and kagome lattices by using the tight-binding model with a general Hamiltonian that describes both lattices by means of only one control parameter. Our findings show that such deformations do not open an energy gap in their electronic spectra but can cause (i) approximation of the energy cones, (ii) anisotropy in the energy levels, and (iii) deformation of the flat band, such that the triply degenerate Dirac point in the Lieb lattice transforms into two doubly degenerate Dirac points. By analyzing hypothetical strain cases in which the values of the hopping parameters do not change, we observe that effects such as deformation in the flat band and division of the triply degenerate Dirac point are only due to the hopping parameter changes caused by the strain. Moreover, we identify cases in which there are non-null strain-induced pseudovector potentials in Lieb and kagome lattices.

DOI: 10.1103/PhysRevB.108.125433

I. INTRODUCTION

The discovery of many interesting properties of two-dimensional (2D) crystals has led in recent years to renewed interest in the study of structures such as the Lieb and kagome lattices. In these systems a conical Dirac energy band coexists with a flat (nondispersive) band. The development of experimental techniques for the synthesis of electronic and chemical structures with such lattice configurations has motivated research on electronic-based lattices [1,2], waveguide-based photonic systems [2–12], and even structures formed by organic bonds [13–24]. In this context this review paper [25] presents some such artificial kagome materials connecting the theoretical ideas and experimental observations, as well as the bond between quantum interactions within kagome magnets and kagome superconductors, and their relation to the concepts in topological insulators, topological superconductors, Weyl semimetals, and high-temperature superconductors, whose topics are at the cutting edge of research into topological quantum matter. Such experiments have allowed the verification of theoretical predictions [26–28], such as the coexistence of Dirac-like cones and flat bands [29–33], and have encouraged theoretical investigations of the effects of deformation on the optoelectronic and magnetic properties of these structures. Recently, there have been investigations of the stability of the flat band and the band-touching points due to breathing anisotropy [34] and disordered flat bands in the kagome lattice [35], as well as multifunctional twisted-kagome lattices [36], strain-induced topological magnon phase transitions [37], and strain-induced pseudomagnetic fields in kagome crystals [38]. Similar studies have explored the dispersion relations of strained and complex Lieb lattices [39] and strain-induced superconductor-insulator transitions on a Lieb lattice [40].

In addition, it has been shown that the Lieb and kagome lattices are interconvertible by applying strain along the diagonal direction [15,16,41–44]. So far there is a lack of studies that present a generic tight-binding Hamiltonian that describes the effect of strain on both Lieb and kagome lattices. References [15,16,41–44] include strain applied along the diagonal direction of the lattice in order to induce the interconvertibility between Lieb and kagome lattices. These studies have demonstrated that a generic lattice (defined in Sec. SI of the Supplemental Material [45]) has a unit cell composed of three sites at the basis (labeled as A, B, and C), which, according to the angle choice ranging from $\pi/2 \leqslant \theta \leqslant 2\pi/3$, corresponds to the Lieb ($\theta = \pi/2$), transitions ($\pi/2 < \theta < 2\pi/3$), and kagome ($\theta = 2\pi/3$) lattices (Fig. 1). But no strain tensor is used in the Hamiltonian, such that diagonal strains are used as a thought experiment, not being explicit in the methodology of these articles. A tight-binding Hamiltonian with the presence of the strain tensor was reported in Ref. [38] but only for the study of strained kagome lattices. However, the authors did not use the knowledge of the interconversibility of Lieb and kagome lattices, which would allow a comparison between the strained Lieb and kagome lattices. Thus, as an extension of the previous studies, in this work we present a general tight-binding Hamiltonian that not only describes

*wellisson@fisica.ufc.br
†diego_rabelo@fisica.ufc.br
‡silviahelena@unilab.edu.br
§pereira@fisica.ufc.br

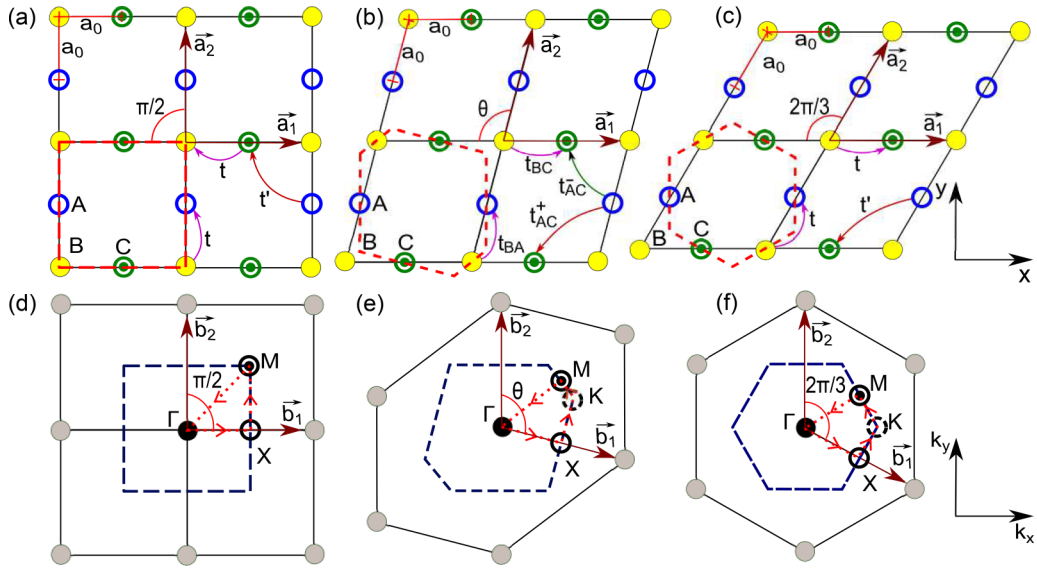

FIG. 1. Real (top panels) and reciprocal (bottom panels) generic lattices: (a) Lieb lattice, (b) transition lattice, and (c) kagome lattice. The primitive vectors are $\vec{a}_1 = a\hat{v}_1$ and $\vec{a}_2 = a\hat{v}_2$, with $\hat{v}_1 = (1, 0)$ and $\hat{v}_2 = (-\cos\theta, \sin\theta)$. The unit cells are denoted by the red dashed lines containing the three nonequivalent sites A (blue open circle), B (yellow filled circle), and C (green circle with dot inside). The distance between nearest-neighbor sites is $a_0 = a/2$ ($a = 1$ Å), and the non-null hopping parameters are represented by t_{BA}, t_{BC}, t^-_{AC}, t^+_{AC}. For Lieb and kagome lattices, the nearest-neighbor hopping is $t_{BA} = t_{BC} = t = 1.0$ eV and the next-nearest-neighbor hopping is $t^-_{AC} = t^+_{AC} = t'$. The first Brillouin zone of the (d) Lieb, (e) transition, and (f) kagome lattices are denoted by the dashed blue lines. The reciprocal vectors are $\vec{b}_1 = b_1\hat{v}_1$ and $\vec{b}_2 = b_2\hat{v}_2$, with $\hat{v}_1 = (\sin\theta, \cos\theta)$ and $\hat{v}_2 = (0, 1)$. The high-symmetry points in the first Brillouin zone are $\vec{\Gamma} = (0, 0)$ (filled circle), $\vec{X} = (b/2)\hat{v}_1$ (open solid circle), $\vec{M} = (b/2)(\hat{v}_1 + \hat{v}_2)$ (circle with dot inside), and $\vec{K} = (1/2)(b - l\cos\theta)\hat{v}_1 + (l/2)\hat{v}_2$ (open dashed circle), with $l = b/(1 - \cos\theta)$.

the interconvertibility between the Lieb and kagome lattices but also enables the investigation of these structures under strains along various crystallographic directions, according to the strain theory for 2D materials (presented in Sec. SII of the Supplemental Material [45]). Based on this formalism we investigate the effects of strain on the energy spectrum of Lieb and kagome lattices that have not been previously explored, such as (i) the appearance of anisotropy in the energy levels, (ii) the variation of the Fermi level, (iii) strain-induced flat-band deformations, (iv) a shift of the Dirac points with respect to the location of the high-symmetry k-space points, and (v) the appearance of strain-induced pseudovector potentials. In Ref. [38] the pseudovector potential terms originated by strain in the kagome lattice were presented, but the effects caused by such terms on the energy spectrum were not explored. In the present work, on the other hand, we show both the effect of nonzero strain-induced pseudovector potentials on kagome and Lieb lattices and make a comparison between these lattices.

Furthermore, inspired by studies that explore the strain effects on graphene-based systems [46–51], we investigate two theoretical methodologies for applying deformations in Lieb and kagome lattices, namely, real and hypothetical cases [45]. In the former case, we consider that the strain tensor changes the position of the lattice sites, and consequently, it modifies the hopping parameter values that connect the atomic sites. In the latter we admit that the hopping parameters' values remain unchanged, being independent of the applied lattice deformation [52–56]. Six different types of strains are investigated here, which are uniaxial strain along (i) the x direction (UX) [Fig. 2(a)] and (ii) the y direction (UY) [Fig. 2(b)], (iii) biaxial (BI) strain [Fig. 2(c)], simple shear strain along (iv) the x direction (SX) [Fig. 2(d)] and (v) the y direction (SY) [Fig. 2(e)], and (vi) pure shear (PS) strain [Fig. 2(f)]. In the hypothetical case, the labels are denoted with the subscript h, such as UX_h, UY_h, BI_h, SX_h, SY_h, and PS_h [45].

The paper is organized as follows. In Sec. II we describe the tight-binding model applied to a strained generic lattice. In Secs. III and IV we discuss the strain effects on the Lieb and kagome lattices, respectively. Finally, in Sec. V we summarize our main findings. We also provide Supplemental Material [45] which discusses the following related issues: (Sec. SI) the crystallographic aspects of the Lieb-kagome generic lattice; (Sec. SII) a detailed strain analysis in 2D materials; (Secs. SIII and SIV) the relevance of the hopping renormalization in the tight-binding model; (Sec. SV) the choice of the n parameter associated with the hopping decay ratio and its consequences on the Lieb, transition, and kagome band structures; extra energy spectrum plots for the Lieb lattice under (Sec. SVI) UX and SX strains, and (Sec. SVII) UY and SY strains; (Sec. SVIII) evolution of the flat band at the Γ point for kagome lattice under BI strain; (Sec. SIX) comparative analyzes of the hypothetical strain cases for all six investigated strain types; and (Sec. SX) the existence or not of a non-null strain-induced pseudovector potential.

II. THEORETICAL MODEL

The tight-binding Hamiltonian for the strained generic lattice (derived in Sec. SIII of the Supplemental Material [45]) is

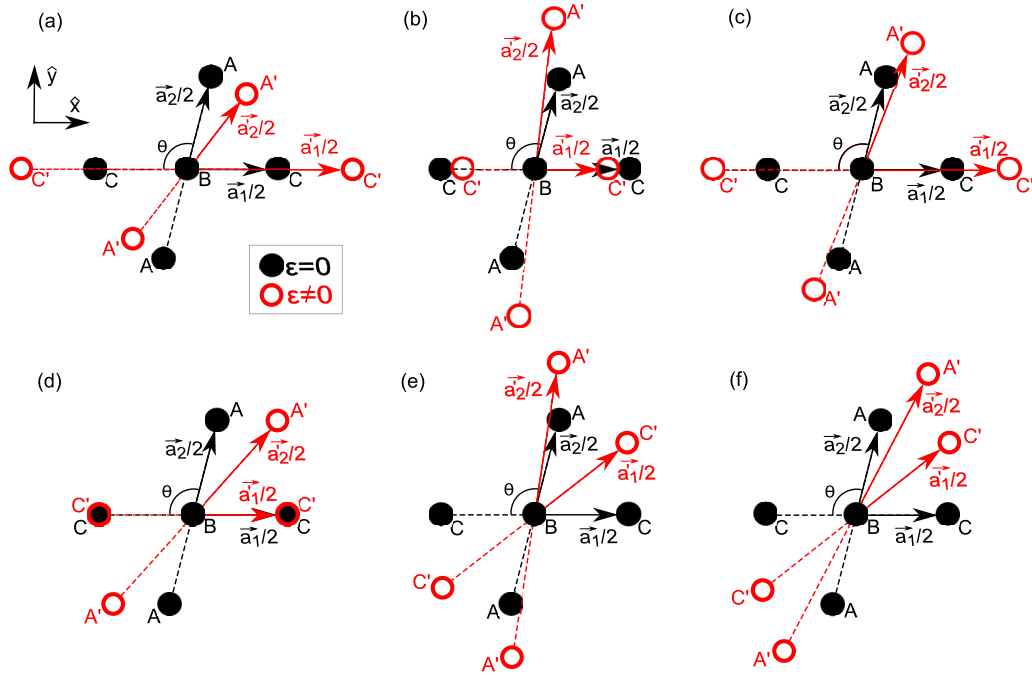

FIG. 2. Comparison of the nonstrained ($\varepsilon = 0$) and strained ($\varepsilon \neq 0$) generic lattices subjected to (a) uniaxial strain along the x direction (UX) and (b) along the y direction (UY), (c) biaxial strain (BI), (d) simple shear strain along the x direction (SX) and (e) along the y direction (SY), and (f) pure shear strain (PS). The generic lattice sites (A, B, and C) are represented by black-filled symbols connected by black dashed lines and primitive vectors $\vec{a}_1$ and $\vec{a}_2$, whereas the strained lattice sites (A′, B′, and C′) are represented by open red symbols connected by red dashed lines and primitive vectors $\vec{a}'_1$ and $\vec{a}'_2$.

given as follows:

$$\hat{\mathcal{H}} = \sum_{jj'}[t'_{BA}(\hat{b}^{\dagger}_{j'}\hat{a}_j + \hat{a}^{\dagger}_j\hat{b}_{j'}) + t'_{BC}(\hat{b}^{\dagger}_{j'}\hat{c}_j + \hat{c}^{\dagger}_j\hat{b}_{j'})] + \sum_{jj'}[t'_{AC}(\hat{a}^{\dagger}_{j'}\hat{c}_j + \hat{c}^{\dagger}_j\hat{a}_{j'})], \quad (1)$$

where $\hat{a}_j$ ($\hat{a}^{\dagger}_j$), $\hat{b}_j$ ($\hat{b}^{\dagger}_j$), and $\hat{c}_j$ ($\hat{c}^{\dagger}_j$) are annihilation (creation) operators corresponding to the jth site of sublattice A, B, and C, respectively.

In our model, as represented in Fig. 2, we consider the hopping energy contributions due to the neighbors located on $\pm\vec{a}'_2/2$, $\pm\vec{a}'_1/2$, $\pm(\vec{a}'_1 - \vec{a}'_2)/2$, and $\pm(\vec{a}'_1 + \vec{a}'_2)/2$, which are denoted as t'_{BA}, t'_{BC}, t'^{-}_{AC}, and t'^{+}_{AC}, respectively. These hopping parameters follow the transformation (described in Sec. IV of the Supplemental Material [45])

$$t'_{ij} = te^{-n(a'_{ij}/a_0-1)}a_0/a'_{ij}, \quad (2)$$

where $n = 8$, and a'_{ij} represents the distance between the atomic sites i and j in the strained lattice, which is given with respect to the undeformed lattice distances a_{ij}, according to $\vec{a}'_{ij} = (\mathbb{I} + \bar{\varepsilon})\vec{a}_{ij}$ with $a'_{ij} = (\vec{a}'_{ij} \cdot \vec{a}'_{ij})^{1/2}$, since

$$\bar{\varepsilon} = \begin{pmatrix} \varepsilon_{xx} - \sigma\varepsilon_{yy} & \varepsilon_{xy} \\ \varepsilon_{yx} & \varepsilon_{yy} - \sigma\varepsilon_{xx} \end{pmatrix}, \quad (3)$$

where $\sigma = 0.1$ denotes the Poisson ratio [46]. Thus the correspondence of the atomic positions of the strained lattices, $\vec{r}' = (r'_x, r'_y)$, with the nonstrained lattice sites, $\vec{r} = (r_x, r_y)$, is given by [57,58]

$$\begin{pmatrix} r'_x \\ r'_y \end{pmatrix} = \begin{pmatrix} [1 + (\varepsilon_{xx} - \sigma\varepsilon_{yy})]r_x + \varepsilon_{xy}r_y \\ \varepsilon_{yx}r_x + [1 + (\varepsilon_{yy} - \sigma\varepsilon_{xx})]r_y \end{pmatrix}, \quad (4)$$

with ε_{ij} values (with $i, j = x, y$) being summarized in Table I for all six investigated deformations.

From Eq. (2) it is seen that the hopping energy decreases as the value of the n parameter increases. Thus the n parameter governs the range of interactions between the atomic sites. That is, the effects of more distant sites are suppressed for $n \geqslant 8$ and intensified for $n < 8$. Figures S1 and S2 of the Supplemental Material [45] show that for $n = 8$, the energy bands give a good approximation of the characteristic of the Lieb and kagome lattices within the nearest-neighbor tight-binding model, since they present almost flat bands and Dirac cones, as expected for such structures [42]. A detailed discussion is presented in Sec. SV of the Supplemental Material [45].

TABLE I. Strain tensor elements [Eq. (3)] for each type of strain applied in Lieb and kagome lattices.

Type of strain	ε_{xx}	ε_{xy}	ε_{yx}	ε_{yy}
UX	ε	0	0	0
UY	0	0	0	ε
BI	ε	0	0	ε
SX	0	ε	0	0
SY	0	0	ε	0
PS	0	ε	ε	0

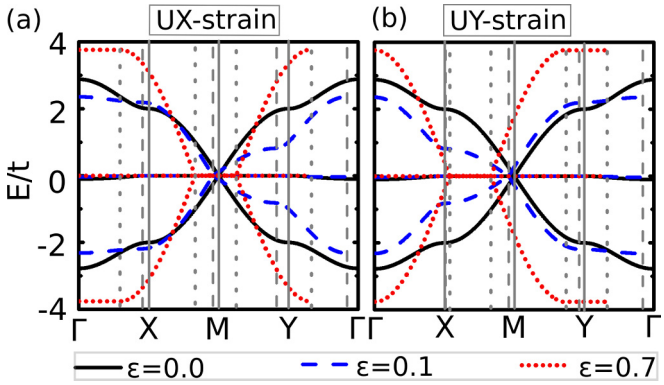

FIG. 3. Band structures along the high-symmetry path $\vec{\Gamma} - \vec{X} - \vec{M} - \vec{Y}(= \vec{b}_2/2) - \vec{\Gamma}$ in the first Brillouin zone of Lieb lattice submitted to (a) UX and (b) UY strains for different strain amplitudes: $\varepsilon = 0.0$ (solid black), $\varepsilon = 0.1$ (dashed blue), $\varepsilon = 0.7$ (dotted red). Vertical gray lines with their respective line styles linked to the ε value indicate the position of the high-symmetry points for $\varepsilon = 0.0$ (solid), $\varepsilon = 0.1$ (dashed), and $\varepsilon = 0.7$ (dotted).

III. STRAINED LIEB LATTICE

In Fig. 3(a) [3(b)], we illustrate the dispersion relation along the path connecting the high-symmetry points $\vec{\Gamma} - \vec{X} - \vec{M} - \vec{Y} - \vec{\Gamma}$ in the reciprocal space of the strained Lieb lattice under UX strain [UY strain] for various strain amplitudes. The isoenergy curves corresponding to the upper (right panels), middle (middle panels), and lower (left panels) bands for the UX-strain case are depicted in Fig. 4. The corresponding case for UY strain is shown in Fig. S5 of the Supplemental Material [45].

Note that the energy spectrum shows electron-hole symmetry even with the strain application. By varying the ε parameter, one notices that if $\varepsilon > 0$ ($\varepsilon < 0$) the Dirac cones approach (move away) the $\vec{M} - \vec{Y}$ direction, i.e., along the $\vec{k}_x$ direction (Fig. 4), and the $\vec{X} - \vec{M}$ direction, i.e., along the $\vec{k}_y$ direction (Fig. S5) [45], for UX-strain and UY-strain cases, respectively. As seen in Figs. 3(a) and 3(b), such uniaxial strains do not cause an energy-gap opening, regardless of the application direction. Instead of the appearance of an energy gap, as shown in strained graphene [46], the Lieb lattice under uniaxial strain presents the formation of a triply degenerate linear band, i.e., a Dirac line, at the Fermi level along the $\vec{M} - \vec{Y}$ direction for the UX-strain case and along the $\vec{X} - \vec{M}$ direction for UY-strain case, as shown by the red dashed curves in Figs. 3(a) and 3(b), respectively. This also can be verified in the fifth row (for $\varepsilon = 0.3$) of contour plots in Fig. 4 and in Fig. S3(d) [45] for the UX-strain case, and in the first row (for $\varepsilon = -0.3$) of contour plots in Fig. S5 [45] for the UY-strain case. Thus one has a type-III Dirac point (critically tilted) that combines flat-band and linear dispersion, similar to cones emerging from flat bands in photonic orbital graphene [59]. This triply degenerate Dirac strain-induced line state is formed by the approach (separation) of the Dirac cones, which, in turn, is accompanied by a small decrease (increase) in the separation and curvature of the upper and lower energy bands in the energetic line that connects the cones along the k_x (k_y) direction, for a fixed k_y (k_x) near to the first Brillouin

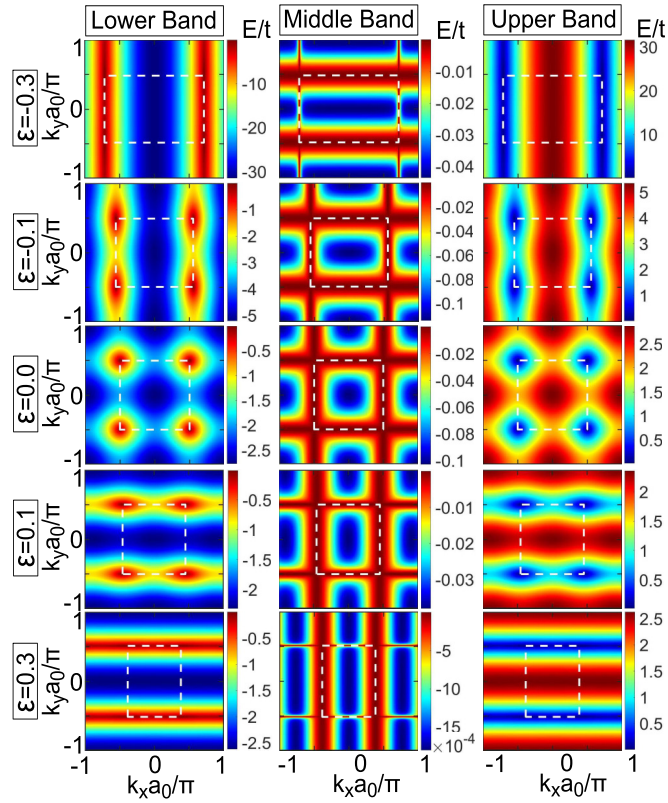

FIG. 4. Contour plots of the lower (left panels), middle (middle panels), and top (right panels) energy bands for Lieb lattice under UX strain for different strain amplitudes: $\varepsilon = -0.3,\ -0.1,\ 0.0,\ 0.1,\ 0.3$ from top to bottom panels.

boundaries for the UX-strain (UY-strain) cases. This trend of the triply degenerate linear band formation can be noticed by comparing panels (b), (c), and (d) in Fig. S3 [45] for the UX-strain case. This evolution of the UX(UY)-strain-induced band deformation increases the energetic distances between the upper and lower bands along the k_y (k_x) direction, for a fixed k_x (k_y) value, reaching the larger value at the $\vec{\Gamma}$ point.

As expected, the dispersion relations in Fig. 4 (Fig. S5 [45]) are compressed (extended) along the k_x (k_y) direction by taking UX(UY)-strain amplitudes with positive $\varepsilon > 0$ and oppositely for negative $\varepsilon < 0$ values. In addition, one notices small band distortions along the k_y (k_x) direction due to the considered Poisson ratio, as a less expressive response in the opposite applied strain direction. The consequence of these effects is the flattening of the cones along the k_y (k_x) direction such that they no longer exhibit circular isoenergy curves but rather have approximately elliptical shape [see second and fourth panel rows of the contour plots in Fig. 4 (Fig. S5 [45]) for lower and top bands, respectively, for UX(UY)-strain case]. This leads to anisotropic Fermi velocities, resulting in anisotropic transport properties that may be relevant to direction-dependent electronic transport devices similar to 2D anisotropic semiconductors such as phosphorene [60]. It is worth mentioning that an equivalent direct analysis between the results under the UX-strain and UY-strain cases can be easily achieved by taking the following transformation: $\vec{k}_x \to \vec{k}_y$ and $x \to y$ for the reciprocal and real spaces, re-

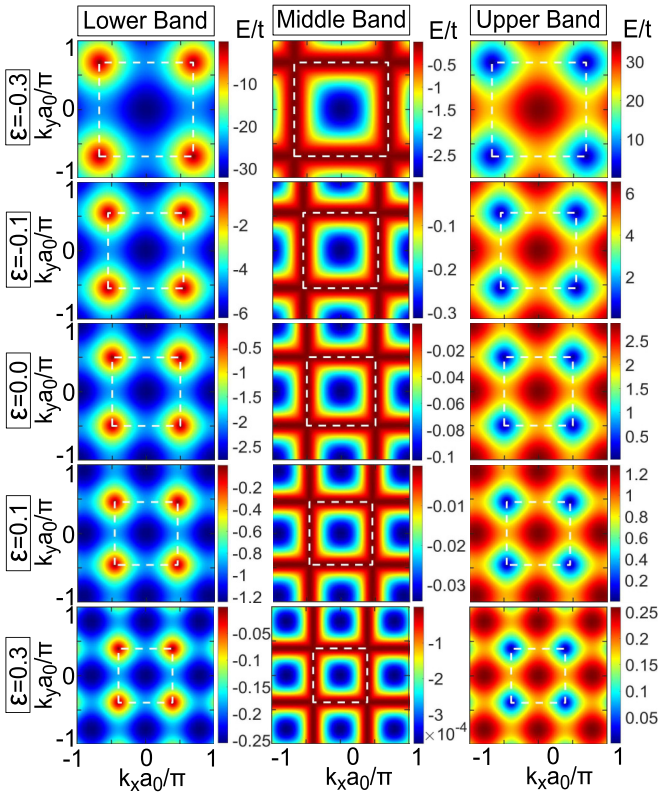

FIG. 5. The same as in Fig. 4, but now for the Lieb lattice under BI strain.

spectively. This is due to the fact that Lieb lattice obeys $\hat{D}_{4h}$ symmetry. Therefore compression ($\varepsilon < 0$) and extension ($\varepsilon > 0$) for UX strain can be mapped by extension and compression, respectively, for the UY-strain case. This statement can be verified by the correspondence between the panels of the following rows: $1_{UX} \longleftrightarrow 5_{UY}$, $2_{UX} \longleftrightarrow 4_{UY}$, $4_{UX} \longleftrightarrow 2_{UY}$, and $5_{UX} \longleftrightarrow 1_{UY}$ for Fig. 4 $\longleftrightarrow$ Fig. S5 [45].

In contrast to the real UX- and UY-strain cases in the Lieb lattice, as shown in Figs. 4 and S5 [45], for both corresponding hypothetical cases UX_h and UY_h presented in Fig. S8 of the Supplemental Material [45], it can be observed that (i) the flat band remains undeformed, maintaining the same energy scale as the color bar, and (ii) the deformed upper and lower bands in the hypothetical strained cases do not give rise to the triply degenerate Dirac strain-induced line state [45].

In order to verify additive effects due to the combination of uniaxial strains along x and y directions, viewed as biaxial deformations, Fig. 5 shows the band structures of Lieb lattice under BI strain for the same strain amplitudes adopted in Fig. 4. Regardless of the strain amplitude, it is seen in Fig. 5 that the bands' curvatures and their aspect ratios in k space are kept undeformed, keeping the circular symmetry of the contour lines close to the Fermi level, which indicates that the Fermi velocity remains isotropic under BI strain. This is easily understood, given that the high-symmetry points are also shifted uniformly in both directions in the BI strain as a consequence of the modules' increase (decrease) of the two lattice vectors for extension $\varepsilon > 0$ (compression $\varepsilon < 0$), leading to the modules' reduction (increasing) of the two reciprocal lattice vectors and also to a smaller (larger) first square Brillouin zone.

In contrast to the real BI-strain case (Fig. 5), where the bands deform in such a way that the color bar range is clearly altered, resulting in a maximum energy scale ten times greater than the unstrained case, this is not the case for the Lieb lattice with BI_h strain. In Fig. S9 of the Supplemental Material [45], it can be observed that the energy scale on the color bar remains unchanged for any strain value and for any of the three bands. This can be easily understood by the fact that we are imposing changes in the lattice structure without considering any modifications in the hopping parameters, which in turn, prevents alterations in the energy scale of the bands [45].

Analyzing the Dirac cone position in the reciprocal space for Lieb lattice under uniaxial and biaxial strains in Fig. S14 of the Supplemental Material [45], one notes that the results for both hypothetical and real strain cases exhibit the Dirac point coinciding with the $\vec{M}'$ point. This means that such strain types in the Lieb lattice do not require correction terms to make matching the position of the Dirac points and the $\vec{M}'$ point of the strained reciprocal lattice, and consequently, no vector pseudopotential is expected, i.e., $\vec{A} = 0$ [45].

Let us now analyze the energy spectrum of the Lieb lattice subjected to shear strain. For SX strain, Fig. 6 shows that the triply degenerate Dirac point at Fermi energy level in the vicinity of the M point gives place to two pairs of doubly degenerated Dirac points. The larger the strain amplitude, the more noticeable is the formation of these two pairs of doubly degenerate Dirac points, which arises from the deformation of the flat band, without a band-gap opening, adjusting itself to touch a pair of points in the upper energy band and a pair of points in the lower energy band. This is clearly shown in the three-dimensional plots [Figs. S4(a) and S4(b)] of the Supplemental Material [45], and through the band evolution in Fig. 6 and the Brillouin zone (white dashed line) distortion by increasing ε value. Moreover, the connecting energetic lines between the pair of doubly degenerate points in the upper bands and in the lower bands, which are initially perpendicular in k space, for high ε values tend to be aligned in k space, and these double Dirac points move away from each other. This can be clearly seen in Figs. S4(c) [45] and S4(d) [45] for $\varepsilon = 0.5$. From these results (Figs. 6 and S4) it becomes evident that the flat band plays an important role as it deforms, creating four Dirac points that do not allow the band gap to open. Reference [43] explores the emergence of Dirac points from flat bands in generic lattices of Lieb and kagome during their interconversibility process. This can be understood in view of the fact that diagonal deformations inherent to the interconversibility process result in structures that can be achieved with a combination of shear and uniaxial deformations.

A particular observation can be noticed on the SX-strained case for $\varepsilon = 0.5$ (Figs. S4(c) [45] and S4(d) [45]). For this strain amplitude, the x components of the vectors that locate the A sites in relation to the B sites have exactly half of the distance value that separates the $B - C$ sites. However, perhaps as expected by the analysis of the triangle BAC formed by the sublattices A, B, and C, this strain situation does not lead to the case of the kagome lattice. This is due to the fact

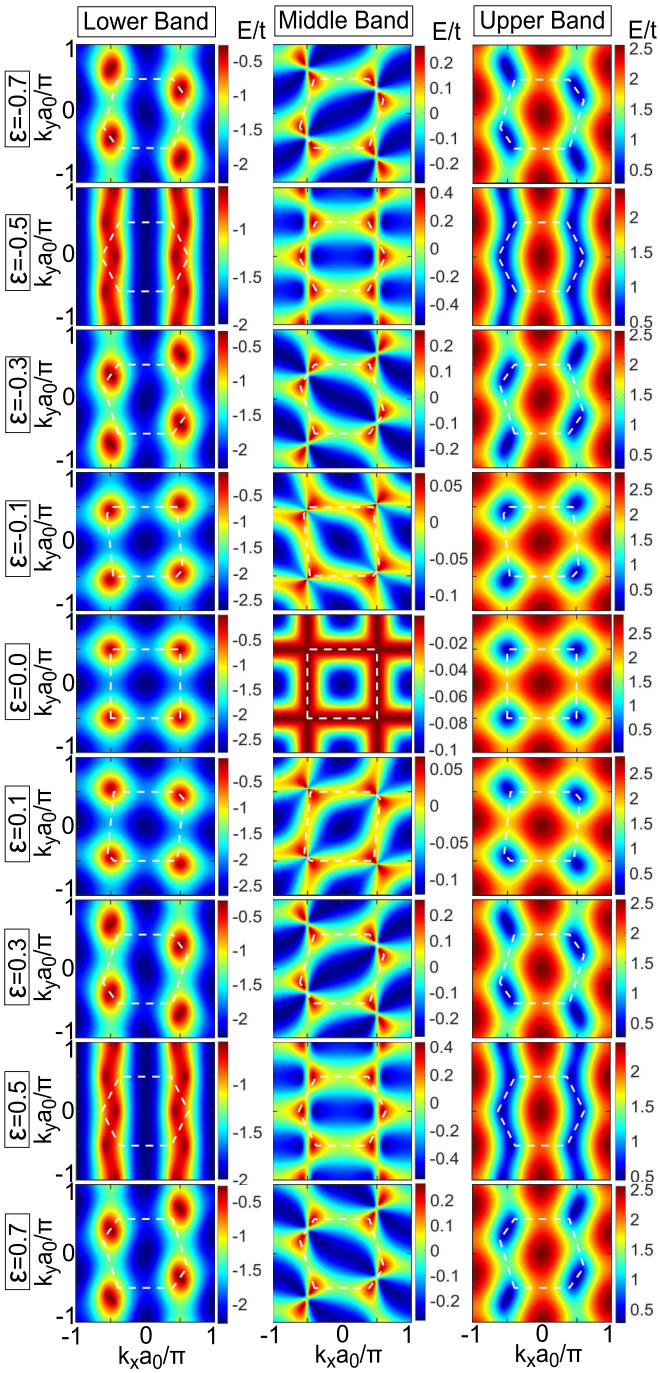

FIG. 6. The same as in Fig. 4, but now for the Lieb lattice under SX strain and assuming the following order of the strain amplitudes: $\varepsilon = -0.7,\ -0.5,\ -0.3,\ -0.1,\ 0.0,\ 0.1,\ 0.3,\ 0.5,\ 0.7$ from top to bottom panels. The strain cases with $\varepsilon > 0$ and $\varepsilon < 0$ are enantiomorphs in absolute values of ε.

that a simple shear strain in x direction does not change the y coordinate of the vector that locates the A sublattice, and thus it does not form an equilateral triangle BAC, which in turn does not correspond to the spatial configuration referred to the $\theta = 2\pi/3$ case. Therefore, by applying the SX strain in the Lieb lattice with strain amplitude $\varepsilon = 0.5$, one obtains a lattice structure that resembles the kagome lattice compressed uniaxially in the x direction, with some $\varepsilon < 0$, as indicated by the contour plots in the eighth row of Fig. 6. This result further confirms the fact that the Lieb and kagome lattices are interconvertible under diagonal strain, as it is easy to understand geometrically that the combination of uniaxial strain and simple shear strain can generate deformations similar to those caused by diagonal strain. Moreover, notice that for $\varepsilon > 0.5$, the inversion in the orientation of the isoenergy curves is owing to the fact that the A sublattice is closer to the left of sublattice C than the right of sublattice B, generating a spatial configuration of sites that behaves like a simple shear strain with $\varepsilon < 0$, as shown in Fig. 6.

The isoenergy curves for the Lieb lattice under the effect of SY strain are shown in Fig. S6 of the Supplemental Material [45]. Similarly to the SX-strain case (Fig. 6), one notices that the energy spectra for the SY-strained Lieb lattice are very similar to those for a diagonally strained kagome lattice when $\varepsilon = 0.5$ (we shall return to this in Sec. IV). Moreover, one notes the following equivalence between the results under SX strain (Fig. 6) and SY strain (Fig. S6 [45]): transformations in the SX-strained (SY-strained) isoenergies composed by a $\pi/2$ rotation in the k space combined with a compression-to-distension (or vice verse) exchange lead to the same energetic band curves as the SY-strained (SX-strained) Lieb case with a sign change in the strain amplitude ε, i.e., by applying a $\hat{C}_2$ symmetry operation in the momentum space and changing $\varepsilon < 0$ by $\varepsilon > 0$ (or vice versa), one gets the same energy spectrum for Lieb lattice with shear strain applied in the other direction. This statement can be verified by the correspondence between the panels of the following rows of Fig. 6 (SX) and Fig. S6 [45] (SY): $1_{SX} \equiv \hat{C}_2 9_{SY}$ $(9_{SY} \equiv \hat{C}_2 1_{SX})$, $2_{SX} \equiv \hat{C}_2 8_{SY}$ $(8_{SY} \equiv \hat{C}_2 2_{SX})$, $3_{SX} \equiv \hat{C}_2 7_{SY}$ $(7_{SY} \equiv \hat{C}_2 3_{SX})$, $4_{SX} \equiv \hat{C}_2 6_{SY}$ $(6_{SY} \equiv \hat{C}_2 4_{SX})$.

Therefore it becomes evident that the cases with $\varepsilon > 0$ and $\varepsilon < 0$ are enantiomorphs in absolute values of ε parameter, i.e., they are mirror images of each other. The energy spectra being enantiomorphs are a consequence of the fact that the displacement of the sites in the simple shear are mirror images of each other for deformations caused by positive and negative values of the ε parameter. The reference line to perform the simple shear must be the same in both cases, and the atoms will move on both sides of the reference line in order to form exactly deformed structures enantiomorphs.

In the Supplemental Material [45], we verified the behavior of the Lieb lattice under simple shear strain in a hypothetical case (Fig. S10). Specifically, we found that the electron-hole symmetry is nearly preserved, and the triple degeneracy of the Dirac point is maintained regardless of the applied strain amplitude and direction. It also observes the absence of the connecting energetic lines between the upper and middle bands and middle and lower bands that are formed for high strain amplitudes when the triply degenerate Dirac cone is divided into two. Notable differences between the hypothetical shear strain cases and the corresponding real cases can be seen by comparing Figs. 6 and S6 [45] for SX and SY strains with Fig. S10 [45] for SX_h and SY_h strains. Therefore the effects of degeneracy breaking and the nonconservation of the electron-hole symmetry in the energy spectrum of the Lieb lattice under simple and pure shear strains are due to the variation of the strain-induced hopping parameters, indicating

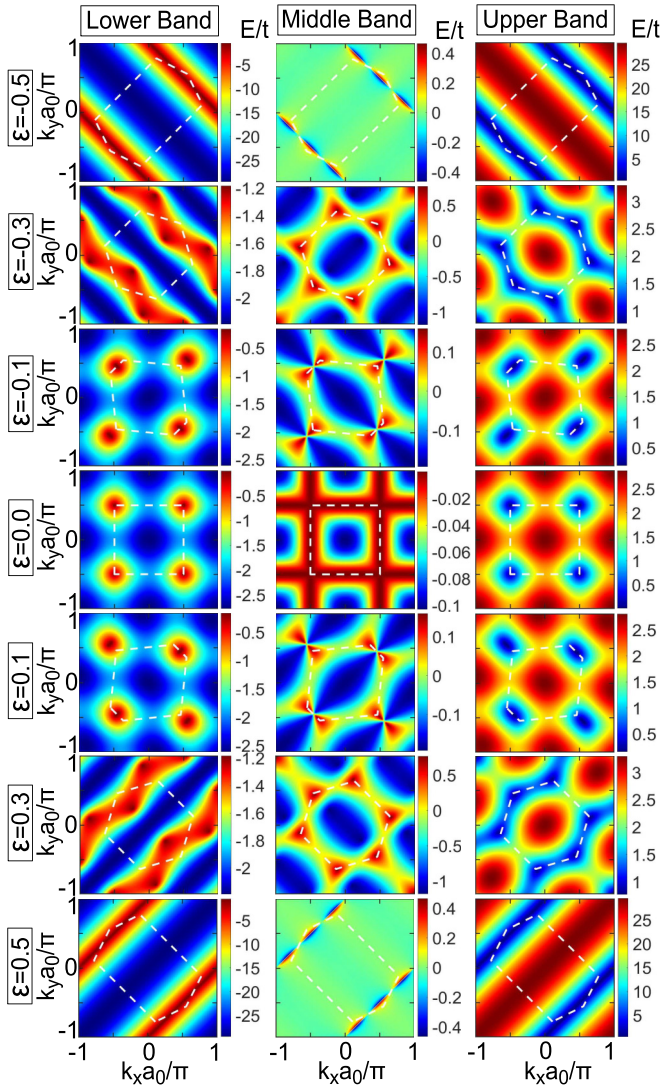

FIG. 7. The same as in Fig. 6, but now for the Lieb lattice under PS strain. Note that the cases for $\varepsilon > 0$ and $\varepsilon < 0$ are mirror images of each other in absolute values of the ε parameter, or equivalently mapped on each other by $\pi/2$ rotation.

a non-null term for the vector potential $\vec{A}$ for the real cases of SX and SY strains [45].

To investigate combined effects due to simple shear strains along the x and y directions, we present in Fig. 7 the band structures of the Lieb lattice under PS strain for the same strain amplitudes adopted in Figs. 6 and S6 [45]. Note that, similarly to the simple shear strain cases, the original triply degenerate Dirac point of the Lieb lattice is split into two doubly degenerate Dirac points. When this occurs, the lower and upper energy bands are divided into two, so the connecting energetic lines between the upper and middle bands and middle and lower bands are always perpendicular, regardless of the applied strain amplitude. This situation is opposite to that discussed cases of simple shear strains, where such two energetic lines connecting the par of doubly degenerate points tend to align with each other. The case corresponding to $\varepsilon = 0.5$ ($\varepsilon = -0.5$), shown in the first (seventh) row of Fig. 7, resembles the energy spectrum of the kagome lattice rotated by $\pi/4$ clockwise (counterclockwise) in relation to to the positive k_x axis.

From Fig. 7 a diagonal deformation is clearly noticeable caused by the PS strain but now without any rotation of the energy spectrum, as observed for the simple shear strain cases (Figs. 6 and S6 [45]). This can be understood by Eq. (4) and Table I, which for the PS-strain case has that $\vec{a}'_1 = (\varepsilon a, 0)$ and $\vec{a}'_2 = (0, \varepsilon a)$, leading to $(\vec{a}'_1)_x = (\vec{a}'_2)_y = \varepsilon a$ and $(\vec{a}'_1)_y = (\vec{a}'_2)_x = 0$, and which consequently sets a diagonal deformation without any isoenergy curve rotation. On the other hand, the rotation of the isoenergy spectrum for simple shear strain cases occurs because, in these cases, $(\vec{a}'_1)_x \neq (\vec{a}'_2)_y$ and $(\vec{a}'_1)_y \neq (\vec{a}'_2)_x = 0$. This discussion also explains the reason why PS-strain results for $\varepsilon > 0$ and $\varepsilon < 0$ are mirror images of each other in absolute values of the ε parameter, i.e., they can be mapped on each other by rotations of $\pi/2$ both clockwise and counterclockwise in relation to the energy axis, which no longer occurs in the simple shear strain cases, whatever the deformation direction.

In the Supplemental Material [45] we demonstrate that, unlike the real PS-strain case (Fig. 7), for a Lieb lattice under hypothetical PS strain (PS_h), (i) the triply degenerate Dirac point at Fermi energy level does not split into two pairs of doubly degenerate Dirac points, and (ii) the electron-hole symmetry is nearly preserved, as noted by the fact that the lower and upper bands obey the following $E_{\text{lower}} = -E_{\text{upper}}$ symmetry and the color-bar scale of the flat band for $\varepsilon > 0$ remains nearly unchanged. Oppositely, one has for the PS-strain case that the lower and upper energy bands are connected to the middle band by energetic lines that are perpendicular between themselves, i.e., between the upper and middle bands and middle and lower bands, reinforcing the symmetry-breaking argument for the real PS-strain case.

IV. STRAINED KAGOME LATTICE

Let us now investigate the effects of the six deformation types illustrated in Fig. 2 and given in Table I on the energy spectrum of the kagome lattice. Figure 8 shows the energy spectrum of the kagome lattice under UX strain. For $\varepsilon > 0$ (distention) the Dirac cones approach and merge, forming an elliptical isoenergy similar to the situation found for graphene [46]. However, unlike the latter, the cones in the kagome lattice approach indefinitely, without opening an energy gap (compare the isoenergies on the fourth and fifth rows of Fig. 8). As ε increases, the Dirac cones approach at the same time that the lower band becomes more dispersive, tending to form a single Dirac cone. This can be noticed by the energy-scale increase on the color bar for the lower bands in Fig. 8 when ε increases. In this process the lower band creates spikes that form Dirac cones with the middle band, to the point where this middle band tends to become flat (also note the energy-scale decrease on the color bar for the middle bands when ε increases), thus resembling the Lieb lattice case. The UX-strained dispersion relation for the kagome lattice (Fig. 8) close to the Fermi level is roughly similar to that for simple shear case applied along the x direction for the Lieb lattice (Fig. 6), as shown in the previous section. These obtained results agree with the evident interconversibility between Lieb

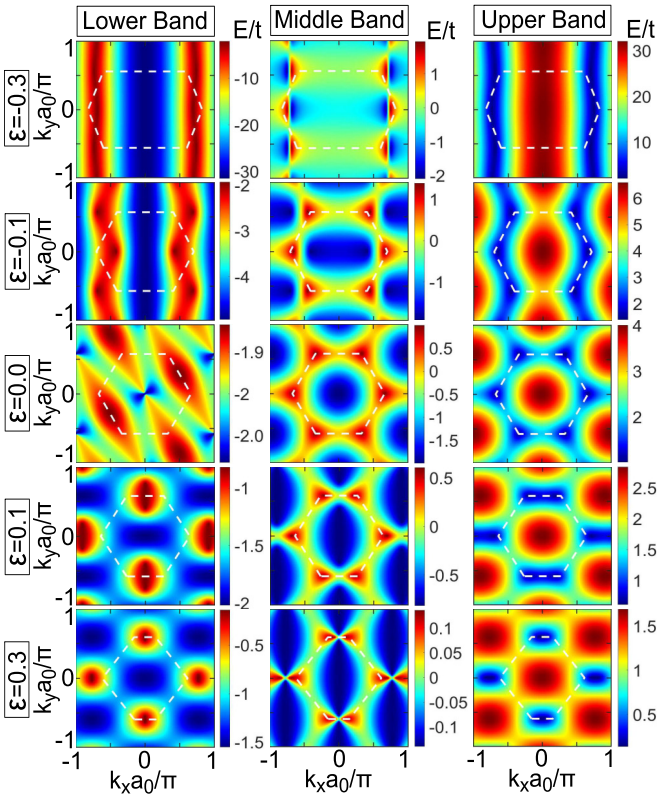

FIG. 8. The same as in Fig. 4, but now for the kagome lattice under UX strain.

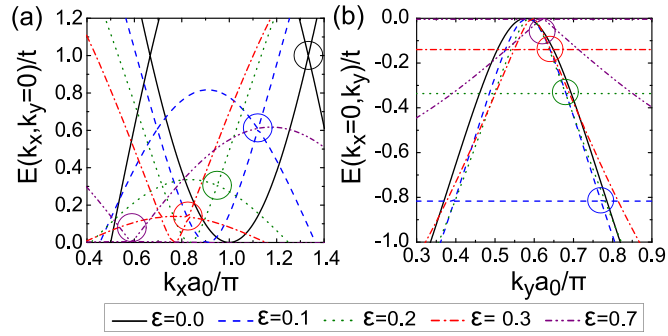

FIG. 9. Dispersion relation of the kagome lattice under UX strain (a) along the k_x direction, keeping $k_y = 0$, and (b) along the k_y direction, keeping $k_x = 0$, for different strain amplitudes: $\varepsilon = 0.0$ (black solid lines), $\varepsilon = 0.1$ (blue dashed lines), $\varepsilon = 0.3$ (green dotted lines), $\varepsilon = 0.5$ (red dash-dotted lines), and $\varepsilon = 0.7$ (purple dash-double-dotted lines). The band crossing is emphasized by circles with the same strained color lines.

and kagome lattices. Furthermore, for $\varepsilon < 0$ (compression), the first and second rows of Fig. 8 show that the Dirac cones move away when the absolute value of ε increases, and consequently, the UX-strained kagome energy spectrum becomes very similar to that displayed by the Lieb lattice under simple shear strain along the x direction (compare with the first row of Fig. 4).

To carefully analyze the approaching behavior of the Dirac cones in the kagome energy spectrum under UX strain, we present in Fig. 9(a) [9(b)] the dispersion relation along the k_x [k_y] direction and keeping $k_y = 0$ [$k_x = 0$] fixed, i.e., it is depicted the spectrum $E(k_x, k_y = 0)$ [$E(k_x = 0, k_y)$], for different strain amplitudes. In Fig. 9(a) one notices that as ε increases, the Dirac cones deform, exhibiting a tilted cone shape with an asymmetric k_x-projected spectrum. As shown in Fig. 9(a), the Dirac cone approximation induced by UX strain results in a total cone immersion when $\varepsilon = 0.7$ (purple dash-double-dotted lines). On the other hand, in Fig. 9(b) one observes an unusual behavior (which brings the flat band to the $E = 0$ level as ε increases) of the Dirac cone formed by the crossing between the dispersive band in the hole region and the flat band. Similar band structure behavior was reported in Refs. [41,43,59,61–64], which explains this energy band evolution as a characteristic behavior of Dirac points emerging from flat bands and merging on flat bands, the latter being the exact case here.

The energy spectra of the kagome lattice under UY strain for the same strain amplitudes as in the UX-strain case (Fig. 8) are depicted in Fig. 10. Because the kagome lattice obeys the $\hat{D}_{6h}$ symmetry, which in turn includes $\hat{C}_2$, $\hat{C}_3$, and $\hat{C}_6$ symmetries, it was expected that UX-strain and UY-strain results would indeed be correlated by, roughly speaking, a $\pi/2$ rotation linked to $\hat{C}_2$ symmetry, except by an energy-scale difference and a size difference on the aspect ratio of the Brillouin zone for each uniaxial strain case (for instance, compare the isoenergies in the first row in Fig. 10 for UY strain and the fifth row in Fig. 8 for UX strain). This aspect ratio difference of the Brillouin zone on k space between

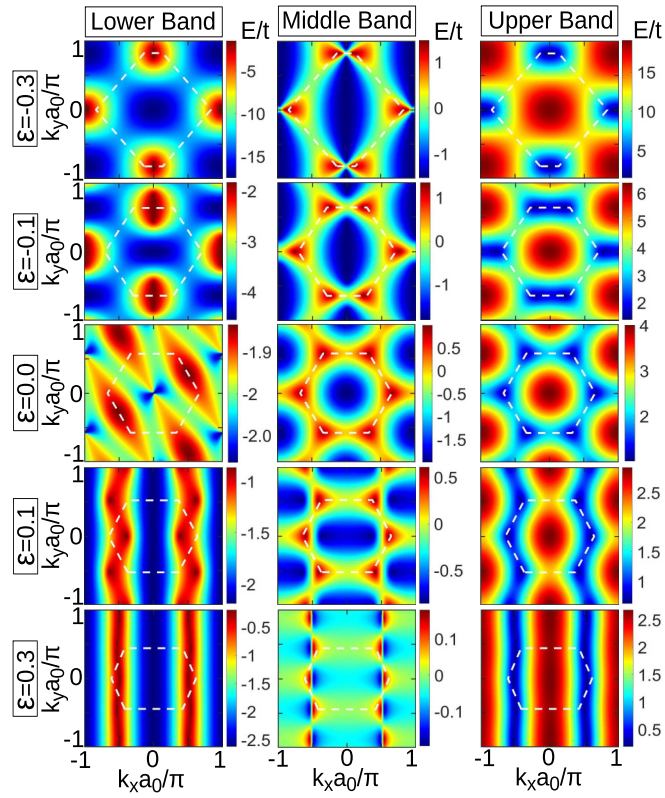

FIG. 10. The same as in Fig. 4, but now for the kagome lattice under UY strain.

UX-strain and UY-strain results for the kagome lattice is linked to the following factors: (i) uniaxial strain causes a larger deformation in the interatomic distances along the applied deformation direction, and (ii) the larger the spatial deformation in a certain direction in the real space the smaller is the Brillouin zone dimension along the corresponding direction. For instance, note that by comparing the $\varepsilon = 0$ (black symbols) with $\varepsilon \neq 0$ (red symbols) illustrations in Figs. 2(a) and 2(b) that the x component of the displacement vectors $\vec{\delta}(\vec{r})$ in Fig. 2(a) is greater than in Fig. 2(b), increasing (decreasing) its modules in the former (latter) situation when one compares the unstrained (black symbols) with the strained (red symbols) cases, which leads to a greater length along the k_x direction of the Brillouin zone for the UY-strain case with $\varepsilon > 0$ in comparison to the UX-strain case with $\varepsilon < 0$. (Compare the isoenergies in the first and second rows in Fig. 8 for UX strain and the fourth and fifth rows in Fig. 10 for UY strain). A similar analysis for the y direction can be done by connecting the distension case ($\varepsilon > 0$) for the kagome lattice under UX strain (Fig. 8) and the compression case ($\varepsilon < 0$) for the kagome lattice under UY strain (Fig. 10), as can be seen by the isoenergies in the fourth and fifth rows in Fig. 8 for UX strain and the first and second rows in Fig. 10 for UY strain. This qualitatively direct analogy is such that compression ($\varepsilon < 0$) and extension ($\varepsilon > 0$) results for the kagome lattice under UX strain can be mapped by extension and compression, respectively, for the UY-strain case. This statement can be viewed by the following correspondence between the rows of Figs. 8 and 10: $1_{UX} \approx 5_{UY}$, $2_{UX} \approx 4_{UY}$, $4_{UX} \approx 2_{UY}$, and $5_{UX} \approx 1_{UY}$.

Unlike the results for the kagome lattice subjected to real uniaxial strains shown in Figs. 8 (UX strain) and 10 (UY strain), in the hypothetical cases (Fig. S11) one observes that (i) the dispersive character of the bands and, consequently, the color-bar-scale ranges are kept unchanged for all three bands, regardless of the strain amplitude and direction; (ii) the approaching of the Dirac cones (for the $\varepsilon > 0$ and UX_h case or for the $\varepsilon < 0$ UY_h case) and the moving away of the Dirac cones (for the $\varepsilon < 0$ and UX_h case or for the $\varepsilon > 0$ UY_h case) are less expressive here than in the real case; (iii) the energetic location of the flat band is not altered in the presence of the hypothetical strain case, whereas in the real UX- and UY-strain cases it approaches the $E = 0$ level as ε increases, as depicted in Fig. 9(b); and (iv) the upper and middle bands are energetically mirror images of each other, and such symmetry is preserved regardless of the strain amplitude and direction. Figures 8 and 10 show that such mirror symmetry between the upper and middle bands is lacking in the real UX- and UY-strain cases. Similarly to the hypothetical cases discussed previously for the Lieb lattice, here for the kagome lattice the absence of the energy-scale change of the bands as well as of the unaltered dispersion character of the bands and the lack of energetic movement of the flat band are due to hypothetical strain not changing the values of the hopping energies. This is an indication that there is a non-null vector pseudopotential term for real UX- and UY-strain cases for the kagome lattice [45].

The additive effects of combined uniaxial strains applied along the x and y directions, i.e., BI strain, in the energy bands of the kagome lattice are shown in Fig. 11. The consequences

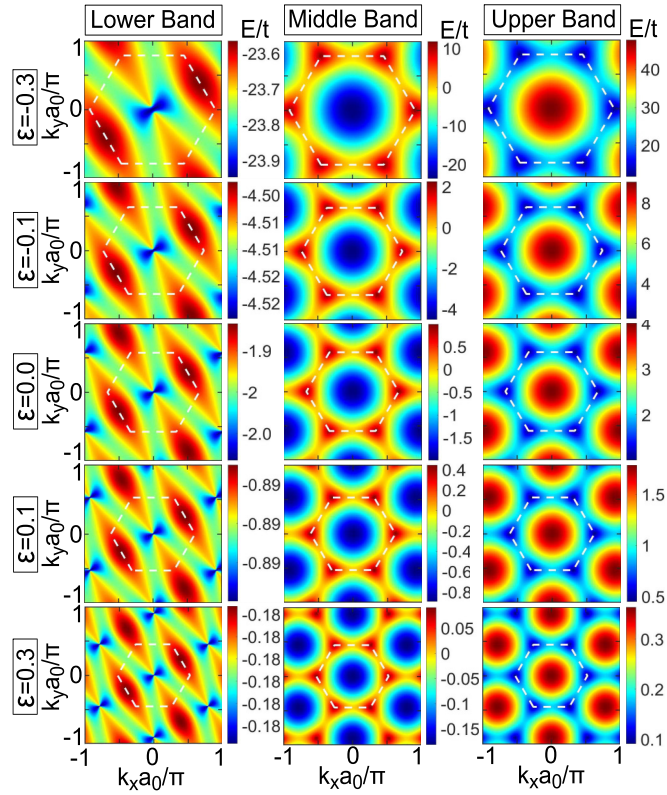

FIG. 11. The same as in Fig. 4, but now for the kagome lattice under BI strain.

on the energy spectrum of the kagome lattice under BI strain are similar to those observed in Fig. 5 for the Lieb lattice subjected to the same strain type: (i) regardless of the strain amplitude, the band curvatures and their aspect ratios in k space are kept undeformed, maintaining in the current case its original hexagonal structure of the unstrained middle and upper bands; and (ii) the biaxial lattice deformation roughly keeps the flat band without dispersion. On the other hand, unlike the Lieb response to BI strain (Fig. 5), the kagome lattice biaxially strained (Fig. 11) presents an energetic shift of the flat band, as verified by the energy-scale change of the lower-band color bar in the left column of Fig. 11 and in Fig. 9(b). As already discussed in Sec. II, due to strain the lattice distances change, and consequently, $t' \equiv t_{ij}$ varies with respect to the ε parameter according to Eq. (2). Thus, by increasing the value of the strain amplitude ε for the BI-strain case, the entire flat band of the kagome lattice (see the left column in Fig. 11) is energetically shifted up (down) along the energy axis for $\varepsilon > 0$ ($\varepsilon < 0$). This behavior is emphasized in Fig. S7 of the Supplemental Material [45], which shows the evolution of the flat band at the Γ point as a function of the (a) strain amplitude ε and (b) the strained hopping parameter t_{ij} expressed in Eq. (2), that for the kagome lattice case corresponds to $t_{ij} \equiv t'$. In Fig. S7(a) [45] one notices that the flat band of the kagome lattice under BI strain obeys an exponential tendency given by the fitting function $E/t = a\exp(b\varepsilon - c) + d$ with $a = -399.9$, $b = 8.359$, $c = 5.328$, and $d = -0.043$, being in concordance with the exponential behavior of the hopping in Eq. (2). Analyzing Fig. S7(b)

[45] one observes a linear dependence of the energy value of the flat band on the t' parameter. This can be understood considering that the energy expression for the flat band in the nondeformed case [65] is given by $E_{\text{flat}} \approx -2t$; thus, in a similar manner it leads to roughly writing an analytical expression for the flat band in the strained kagome case, such as $E_{\text{flat}} \approx -2t'$. This is confirmed by the fitting function of the obtained data given by $E_{\text{fit}} = at' + b$ with $a = -2.014$ and $b = 0.009\,257$.

In the Supplemental Material [45] one observes that the BI_h-strained band curvatures and their aspect ratios in k space are kept unchanged, similarly to the real BI-strain case (Fig. 11), and in addition to that, likewise to each separated hypothetical uniaxial strain case, i.e., to the UX_h and UY_h cases for the kagome lattice shown in Fig. S11 [45], one obtains upper and middle bands obeying an energetic mirror symmetry between themselves without any variation on the energetic scale range for any of the three bands, regardless of the ε value. Such lack of energetic alteration in the BI_h-strained kagome energy bands is equally explained, as in the previous hypothetical cases, in view of there being no changes in the hopping parameters to be considered.

The isoenergy spectra obtained by applying shear strain along the x direction (SX strain) and along the y direction (SY strain) in the kagome lattice are shown in Figs. 12 and 13, respectively. By a careful analysis of Fig. 12, one realizes that, similarly to the Lieb lattice subjected to SX strain (Fig. 6), the strained isoenergies corresponding to distension ($\varepsilon > 0$) and compression ($\varepsilon < 0$) deformations are enantiomorphs in absolute values of the ε parameter, i.e., they are mirror images of each other (compare the first, second, third, and fourth rows of Fig. 12 with the ninth, eighth, seventh, and sixth rows of Fig. 12, respectively). This is due to the isotropic lattice structure of the kagome lattice under shear strain for positive and negative values of the ε parameter, which has its atomic positions deformed oppositely to both sides with respect to an atomic reference line in the lattice (see a similar discussion in the ante-penultimate paragraph in Sec. III for the Lieb lattice under shear strain). Furthermore, the kagome lattice under SX strain with $\varepsilon = 0.5$ roughly resembles the undeformed Lieb lattice, and the undeformed kagome lattice roughly resembles the Lieb lattice under UY strain together with a weakly applied simple shear strain. Although this geometric argument is coherent with respect to the equivalence between these lattice structures, the energy spectra for these two situations are not fully equivalent. On the contrary, it is observed that the obtained isoenergy spectra of the deformed kagome lattice under SX strain (Fig. 12) qualitatively resemble the deformed spectra of the Lieb lattice under SY strain (Fig. S6). For instance, note the similarities between the results of the lower, middle, and upper bands in the fifth and sixth rows of Fig. 12 and the corresponding ones in Fig. 6 for $\varepsilon = 0.3$ and $\varepsilon = 0.5$. On the other hand, for high strain amplitudes (see the ninth row of Fig. 12 for $\varepsilon = 0.7$), the Brillouin zone (white dashed lines) of the kagome lattice under SX strain is no longer a six-sided polygon but rather a parallelogram. In the evolving process of Brillouin zone deformation into a parallelogram, the flat (lower) band becomes more dispersive while the middle band becomes less dispersive, leading to a displacement of the doubly degenerate Dirac points such that

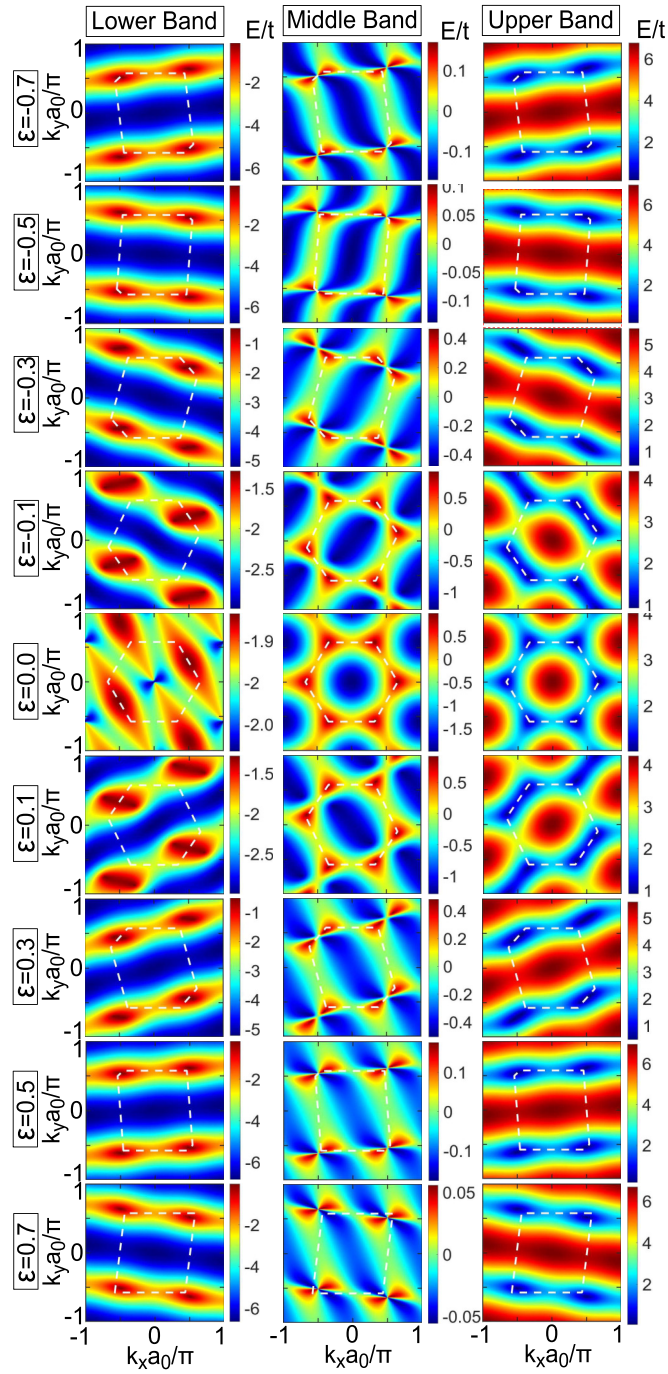

FIG. 12. The same as in Fig. 6, but now for the kagome lattice under SX strain.

for high ε values, these doubly degenerate Dirac points start to merge two-by-two, connecting the high-symmetry points in a parallelogram format.

For the kagome lattice under SY strain, the isoenergies shown in Fig. 13 present a very distinct behavior as compared to the previous SX-strain case (Fig. 12). Due to the lattice deformation caused by the SY strain applied in the kagome lattice, the band structure is strongly affected, becoming highly (less) dispersive for the lower and middle (upper) bands (compare the energy-scale changes on the color bar

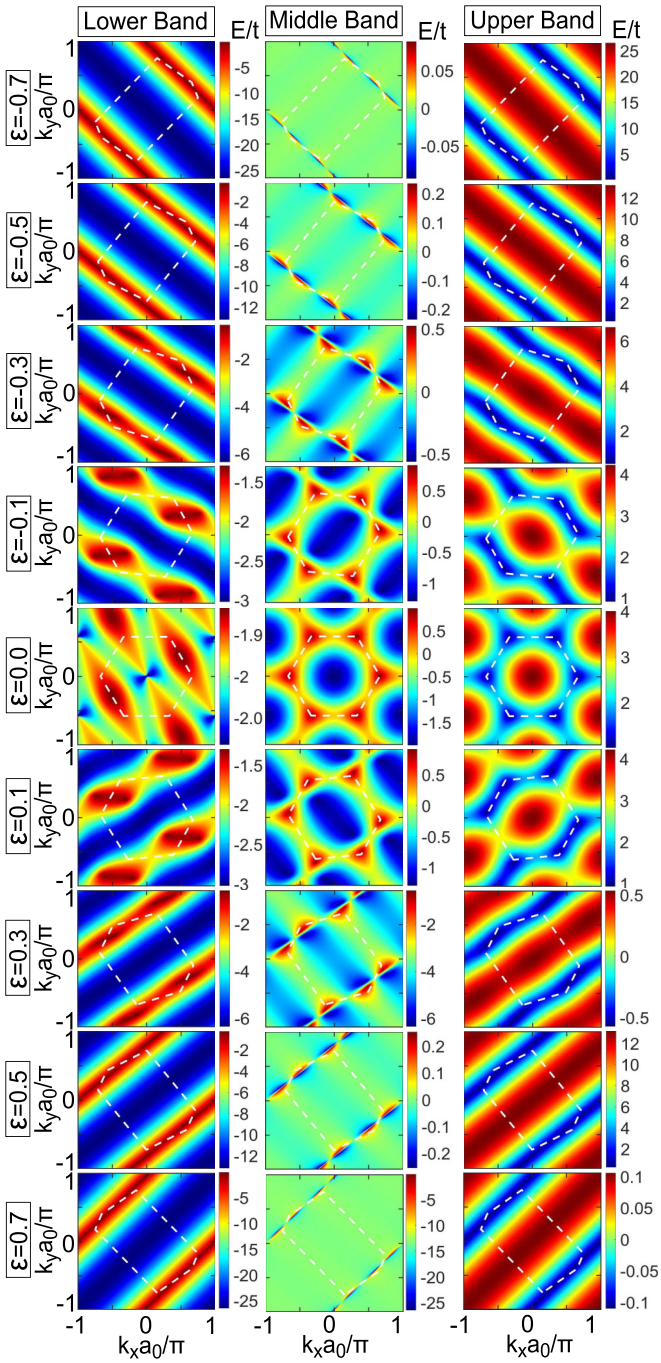

FIG. 13. The same as in Fig. 6, but now for the kagome lattice under SY strain.

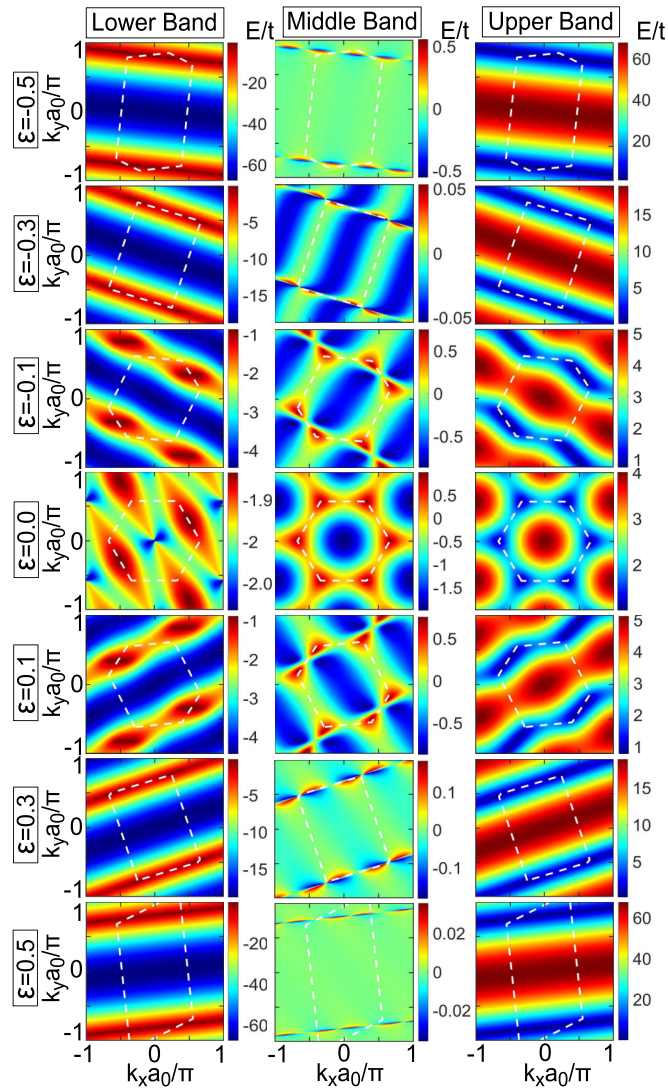

FIG. 14. The same as in Fig. 7, but now for the kagome lattice under PS strain.

in Fig. 13). One also observes the doubly degenerate points located at the high-symmetry points in the Brillouin zone being flattened and thus forming energetic lines connecting these degenerate points. Energetically speaking, similar features as those obtained in Fig. 13 for a deformed kagome lattice under SY strain are roughly observed: (i) in the case of the Lieb lattice under pure shear strain (PS strain) subjected to high-strain amplitudes, as can be verified by comparing the seventh row of Fig. 7 for $\varepsilon = 0.5$ with the eighth row in Fig. 13, and (ii) when the kagome lattice is subjected to uniaxial strain along the y direction (UY strain), as shown in Fig. 10, but being oriented diagonally in the reciprocal space.

By a direct comparison between Fig. S13 [45] for hypothetical shear strain SX_h and SY_h cases and Figs. 12 and 13 for SX and SY real cases, respectively, one notices that regardless of the strain amplitude and applied direction, there is no way to get the energetic line in the hypothetical (simple or pure) shear strain cases, as well as the emergence of the doubly degenerate points and the breaking mirror symmetry between the middle and upper bands. In this way we can state that the variation of the hopping parameters due to strain is the main cause of the drastic changes in the real pure and simple shear strained energy spectra, indicating that a non-null vector pseudopotential term should be associated with the real cases of SX and SY strains in the kagome lattice, as discussed in more detail in Sec. SX of the Supplemental Material [45].

In order to verify the combined effects of simple shear strains along x (SX-strain) and y (SY-strain) directions in the kagome lattice, Fig. 14 shows the strained isoenergy spectra subjected to pure shear deformation. One notices that,

unlike the Lieb case subjected to the same strain (Fig. 7) where PS strain just causes a diagonal-like deformation in the isoenergies, the strained kagome isoenergies are not only diagonally deformed but rather present a smoother rotation than those corresponding to simple shear cases in Figs. 12 and 13. According to Eq. (4) and Table I for the PS-strain case and taking the primitive vectors for the kagome lattice, one finds that $(\vec{a}'_1)_x \neq (\vec{a}'_2)_y$ and $(\vec{a}'_1)_y \neq (\vec{a}'_2)_x = 0$. This geometric statement of the deformed lattice vectors for each situation explains the nature of the difference between applying PS strain in Lieb (Fig. 7) and kagome (Fig. 14) lattices, as well as between PS strain and SX and SY strains in the kagome lattice.

The most pronounced difference between the kagome lattice under PS and PS_h strains is the nonformation of the energetic lines connecting the doubly degenerate points located at the high-symmetry points in the Brillouin zone caused by the flattening of the middle band. This is a consequence of the lack of band curvature distortion in the PS_h-strain case by keeping the hopping unchanged.

Generally speaking, no pronounced modification of the dispersion relations of the BI_h and PS_h kagome strained cases, shown in Fig. S12 [45], are observed when compared with the unstrained case, but the isoenergies of such hypothetical cases present huge differences with respect to the real BI (Fig. 11) and PS (Fig. 14) strained kagome cases. By such comparison, we understand that the asymmetry of the middle and upper bands, together with the deformation of the flat band, is also due to the variation of the hopping parameters with the strain, indicating non-null vector pseudopotential terms for BI and PS strains in the kagome lattice.

Our results lead us to write an analytical strain-induced $\bar{\varepsilon}$-dependent pseudovector potential for the kagome lattice based on Ref. [38] such as $\vec{A} \propto n(\bar{\varepsilon}_{yy} - \bar{\varepsilon}_{xx}, \bar{\varepsilon}_{xy} + \bar{\varepsilon}_{yx})$, where $\bar{\varepsilon}_{ij}$ is given by Eq. (3) and the n parameter governs the strain-dependent hopping variation, given by Eq. (2). It is worth mentioning that this $\vec{A}$ expression is the same as that for strained graphene, this analogy being possible due to the hexagonal symmetry shared by the kagome and graphene lattices.

V. CONCLUSIONS

In summary, we systematically studied the effects of strain on the electronic properties of the Lieb and kagome lattices based on a recently proposed tight-binding Hamiltonian reported in Ref. [42] that takes into account the interconversibility between the Lieb and kagome lattices by defining a transition lattice that maps such structures by one control parameter. For this purpose, using the concept of a generic lattice [15,16,42,43] (Sec. SI) and the standard deformation theory (Sec. SII), we derived a more general Hamiltonian, including the strain tensor for studying in-plane deformation effects on the energy spectra of such structures within the elastic and linear deformation regimes (Secs. SIII and SIV).

Initially, we discussed the evolution of the energy spectra of nonstrained Lieb and kagome lattices in view of their lattice interconversibility. The effects that the variation of the n parameter, which governs the variation of hoppings parameters, causes on their energy band structures are also investigated (Sec. SV). We found that $n = 8$ is the appropriate value to resume the known energy spectra of the nonstrained ($\varepsilon = 0$) Lieb and kagome lattices and, in turn, is the one assumed here to investigate the strained cases ($\varepsilon \neq 0$). We verified that for $n < 8$, the effects of second nearest neighbors become more evident, causing distortions on the energy spectra, particularly on the flat band, making it more dispersive. In addition, for the Lieb lattice, the changes of the n parameter (taking $n < 8$) do not move the Dirac point, being located in the $\vec{M}$ point, which is due to the lattice configuration symmetry of the next-nearest-neighbor sites. On the other hand, for the kagome lattice and $n < 8$, the Dirac cone moves away from the $\vec{K}$ point in reciprocal space, and the isoenergies become clearly anisotropic.

In general, we observed some effects analogous to those known in the strained graphene literature, such as the presence of anisotropic Fermi velocity, the approach or separation of the Dirac cones, as well as the existence of strain-induced pseudovector potentials for some types of strain. On the other hand, unlike graphene, the strain in the Lieb and kagome lattices never opens an energy gap. Instead, in general terms, we identified effects such as the deformation of the flat bands, division of the triply degenerate Dirac point in two doubly degenerated Dirac points (in the Lieb lattice), as well as the appearance of a non-null vector pseudopotential terms in some types of strain.

The results showed that the flat band deforms without opening an energy gap for strains applied in the Lieb and kagome lattices. For the cases of UX, UY, and BI strains in the Lieb lattice, the flat band deforms such that the original triply degenerate Dirac point splits into two doubly degenerated Dirac points that shift in opposite directions away from the zero energy level.

In addition, for some cases of strain we found that there are non-null strain-induced pseudovector potentials, such as SX, SY, and PS strains in the Lieb lattice, and UX, UY, SX, SY, and PS strains in the kagome lattice. Thus we conclude that for the Lieb lattice $\vec{A} \propto n(0, \bar{\varepsilon}_{xy} + \bar{\varepsilon}_{yx})$, with $\bar{\varepsilon}_{ij}$ given by Eq. (3) and the n parameter being the one that governs the variation of hopping parameters with the strain [Eq. (2)]. On the other hand, the general expression of strain-induced pseudovector potentials for the kagome lattice must be $\vec{A} \propto n(\bar{\varepsilon}_{yy} - \bar{\varepsilon}_{xx}, \bar{\varepsilon}_{xy} + \bar{\varepsilon}_{yx})$, as demonstrated in Ref. [38].

Furthermore, we find that some strain effects in the energy spectra are due exclusively to the variation of the hopping parameters with the strain. Such effects disappear for the hypothetical case, i.e., when we assume that the strain tensor only modifies the configuration of sites of the real lattices, keeping the hopping parameters unchanged. Examples of this are the deformations in the flat band, the separation of the triply degenerate Dirac point in two doubly degenerated Dirac points (in Lieb lattice), and the formation of the triply degenerate Dirac band with the presence of a type-III Dirac point (critically tilted), combining flat-band and linear dispersions. On the other hand, some effects seem to arise exclusively from deformations in real space, which are maintained in hypothetical cases of strains, such as the approximation or separation of Dirac cones and the asymmetry in the energy-level curves.

We believe that such a systematic study pertinent to the effects of different types of strains applied in 2D lattices with

the coexistence of flat and conical bands is very interesting for understanding the defects' effects on the optoelectronic properties of flat-band 2D systems. These are the 2D materials' electrical and optical properties, and consequently, their band-gap tunability and band deformations can be dictated by strain engineering, being one of the various approaches for the proposals aiming to apply 2D lattices for future 2D device technologies.

ACKNOWLEDGMENTS

The authors are grateful for financial support from the National Council of Scientific and Technological Development (CNPq) and the National Council for the Improvement of Higher Education (CAPES) of Brazil. D.R.C. is supported by CNPq Grants No. 313211/2021-3 and No. 437067/2018-1.

[1] M. R. Slot, T. S. Gardenier, P. H. Jacobse, G. C. P. van Miert, S. N. Kempkes, S. J. M. Zevenhuizen, C. M. Smith, D. Vanmaekelbergh, and I. Swart, Nat. Phys. **13**, 672 (2017).
[2] Z. Li, J. Zhuang, L. Wang, H. Feng, Q. Gao, X. Xu, W. Hao, X. Wang, C. Zhang, K. Wu *et al.*, Sci. Adv. **4**, eaau4511 (2018).
[3] R. A. Vicencio, C. Cantillano, L. Morales-Inostroza, B. Real, C. Mejía-Cortés, S. Weimann, A. Szameit, and M. I. Molina, Phys. Rev. Lett. **114**, 245503 (2015).
[4] R. Shen, L. B. Shao, B. Wang, and D. Y. Xing, Phys. Rev. B **81**, 041410(R) (2010).
[5] D. Guzmán-Silva, C. Mejía-Cortés, M. A. Bandres, M. C. Rechtsman, S. Weimann, S. Nolte, M. Segev, A. Szameit, and R. A. Vicencio, New J. Phys. **16**, 063061 (2014).
[6] S. Mukherjee, A. Spracklen, D. Choudhury, N. Goldman, P. Öhberg, E. Andersson, and R. R. Thomson, Phys. Rev. Lett. **114**, 245504 (2015).
[7] S. Taie, H. Ozawa, T. Ichinose, T. Nishio, S. Nakajima, and Y. Takahashi, Sci. Adv. **1**, e1500854 (2015).
[8] S. Xia, Y. Hu, D. Song, Y. Zong, L. Tang, and Z. Chen, Opt. Lett. **41**, 1435 (2016).
[9] F. Diebel, D. Leykam, S. Kroesen, C. Denz, and A. S. Desyatnikov, Phys. Rev. Lett. **116**, 183902 (2016).
[10] N. Goldman, D. F. Urban, and D. Bercioux, Phys. Rev. A **83**, 063601 (2011).
[11] S. A. Schulz, J. Upham, L. O'Faolain, and R. W. Boyd, Opt. Lett. **42**, 3243 (2017).
[12] Y. Zong, S. Xia, L. Tang, D. Song, Y. Hu, Y. Pei, J. Su, Y. Li, and Z. Chen, Opt. Express **24**, 8877 (2016).
[13] B. Keimer, S. A. Kivelson, M. R. Norman, S. Uchida, and J. Zaanen, Nature (London) **518**, 179 (2015).
[14] S. Reichardt, M. Jurkutat, R. Guehne, J. Kohlrautz, A. Erb, and J. Haase, Condens. Matter **3**, 23 (2018).
[15] B. Cui, X. Zheng, J. Wang, D. Liu, S. Xie, and B. Huang, Nat. Commun. **11**, 66 (2020).
[16] W. Jiang, H. Huang, and F. Liu, Nat. Commun. **10**, 2207 (2019).
[17] M. Nita, B. Ostahie, and A. Aldea, Phys. Rev. B **87**, 125428 (2013).
[18] L. Downie, E. Ardashnikova, C. Tang, A. Vasiliev, P. Berdonosov, V. Dolgikh, M. Vries, and P. Lightfoot, Crystals **5**, 226 (2015).
[19] E. Liu, Y. Sun, N. Kumar, L. Muechler, A. Sun, L. Jiao, S.-Y. Yang, D. Liu, A. Liang, Q. Xu *et al.*, Nat. Phys. **14**, 1125 (2018).
[20] S. Nakatsuji, N. Kiyohara, and T. Higo, Nature (London) **527**, 212 (2015).
[21] W.-m. Zhang, H. Ohta, S. Okubo, M. Fujisawa, T. Sakurai, Y. Okamoto, H. Yoshida, and Z. Hiroi, J. Phys. Soc. Jpn. **79**, 023708 (2010).
[22] O. V. Yazyev, Nat. Phys. **15**, 424 (2019).
[23] M. Cui, Z. He, Y. Tang, and C. Qiu, J. Cryst. Growth **475**, 256 (2017).
[24] T. Ono, K. Morita, M. Yano, H. Tanaka, K. Fujii, H. Uekusa, Y. Narumi, and K. Kindo, Phys. Rev. B **79**, 174407 (2009).
[25] J.-X. Yin, B. Lian, and M. Z. Hasan, Nature (London) **612**, 647 (2022).
[26] L. Onsager, Phys. Rev. **65**, 117 (1944).
[27] E. H. Lieb, Phys. Rev. Lett. **62**, 1201 (1989).
[28] M. Mekata, Phys. Today **56**, 12 (2003).
[29] H. M. Guo and M. Franz, Phys. Rev. B **80**, 113102 (2009).
[30] S. Li, W. X. Qiu, and J. H. Gao, Nanoscale **8**, 12747 (2016).
[31] J. L. Lu, W. Luo, X. Y. Li, S. Q. Yang, J.-X. Cao, X. G. Gong, and H.-J. Xiang, Chin. Phys. Lett. **34**, 057302 (2017).
[32] S. Depenbrock, I. P. McCulloch, and U. Schollwöck, Phys. Rev. Lett. **109**, 067201 (2012).
[33] J.-X. Yin, S. S. Zhang, G. Chang, Q. Wang, S. S. Tsirkin, Z. Guguchia, B. Lian, H. Zhou, K. Jiang, I. Belopolski *et al.*, Nat. Phys. **15**, 443 (2019).
[34] K. Essafi, L. D. C. Jaubert, and M. Udagawa, J. Phys.: Condens. Matter **29**, 315802 (2017).
[35] T. Bilitewski and R. Moessner, Phys. Rev. B **98**, 235109 (2018).
[36] D. B. Liarte, O. Stenull, and T. C. Lubensky, Phys. Rev. E **101**, 063001 (2020).
[37] S. A. Owerre, J. Phys.: Condens. Matter **30**, 245803 (2018).
[38] T. Liu, Phys. Rev. B **102**, 045151 (2020).
[39] Y. Zhang, X. Liu, M. R. Belić, W. Zhong, C. Li, H. Chen, and Y. Zhang, Romanian Rep. Phys. **68**, 230 (2016).
[40] N. Swain and M. Karmakar, Phys. Rev. Res. **2**, 023136 (2020).
[41] K. Asano and C. Hotta, Phys. Rev. B **83**, 245125 (2011).
[42] W. Jiang, M. Kang, H. Huang, H. Xu, T. Low, and F. Liu, Phys. Rev. B **99**, 125131 (2019).
[43] L.-K. Lim, J.-N. Fuchs, F. Piéchon, and G. Montambaux, Phys. Rev. B **101**, 045131 (2020).
[44] J.-P. Lang, H. Hanafi, J. Imbrock, and C. Denz, Phys. Rev. A **107**, 023509 (2023).
[45] See Supplemental Material at http://link.aps.org/supplemental/10.1103/PhysRevB.108.125433 and also the additional references therein, Refs. [66–72], for additional discussions concerning: (SI) the generic lattice, (SII) analysis of strain, (SIII) the tight-binding model, which covers a general description for both Lieb-kagome lattices by means of only one control parameter, (SIV) a discussion on the hopping renormalization, pointing out the differences and similarities concerning the hopping normalization, (SV) a discussion on the choice of the n parameter in the hopping energies to obtain the flat bands, (SVI) extra 3D energy spectra of strained Lieb lattice for UX-strain and SX-strain cases, as well as for (SVII) UY-strain and SY-strain cases, (SVIII) evolution of the flat band at the γ point for

the kagome lattice under Bi strain, (SIX) the hypothetical strain cases, in which the values of the hopping parameters do not change, and (SX) the strain-induced vector pseudopotentials, where we identify the cases in which there are non-null strain-induced pseudovector potentials in Lieb and kagome lattices related to the position changes in the reciprocal space of the high-symmetry points.

[46] V. M. Pereira, A. H. Castro Neto, and N. M. R. Peres, Phys. Rev. B **80**, 045401 (2009).

[47] S. H. R. Sena, J. M. Pereira Jr, G. A. Farias, F. M. Peeters, and R. N. Costa Filho, J. Phys.: Condens. Matter **24**, 375301 (2012).

[48] L. Yang, J. Xiaowei, L. Zhongfan, and L. Zhirong, Nano Res. **3**, 581 (2010).

[49] G. G. Naumis, S. Barraza-Lopez, M. Oliva-Leyva, and H. Terrones, Rep. Prog. Phys. **80**, 096501 (2017).

[50] L.-H. Qu, J.-M. Zhang, K.-W. Xu, and V. Ji, Physica E **60**, 156 (2014).

[51] G. Cocco, E. Cadelano, and L. Colombo, Phys. Rev. B **81**, 241412(R) (2010).

[52] M. Oliva-Leyva and G. G. Naumis, Phys. Rev. B **88**, 085430 (2013).

[53] M. Oliva-Leyva and G. G. Naumis, Phys. Lett. A **379**, 2645 (2015).

[54] M. Oliva-Leyva and C. Wang, J. Phys.: Condens. Matter **29**, 165301 (2017).

[55] A. L. Kitt, V. M. Pereira, A. K. Swan, and B. B. Goldberg, Phys. Rev. B **87**, 159909(E) (2013).

[56] A. L. Kitt, V. M. Pereira, A. K. Swan, and B. B. Goldberg, Phys. Rev. B **85**, 115432 (2012).

[57] N. S. Bandeira, D. R. da Costa, A. Chaves, G. A. Farias, and R. N. Costa Filho, J. Phys.: Condens. Matter **33**, 065503 (2021).

[58] J. S. Nascimento, D. R. da Costa, M. Zarenia, A. Chaves, and J. M. Pereira, Phys. Rev. B **96**, 115428 (2017).

[59] M. Milićević, G. Montambaux, T. Ozawa, O. Jamadi, B. Real, I. Sagnes, A. Lemaître, L. Le Gratiet, A. Harouri, J. Bloch *et al.*, Phys. Rev. X **9**, 031010 (2019).

[60] L. Li, Y. Yu, G. J. Ye, Q. Ge, X. Ou, H. Wu, D. Feng, X. H. Chen, and Y. Zhang, Nat. Nanotechnol. **9**, 372 (2014).

[61] G. Montambaux, L.-K. Lim, J.-N. Fuchs, and F. Piéchon, Phys. Rev. Lett. **121**, 256402 (2018).

[62] G. Montambaux, F. Piéchon, J.-N. Fuchs, and M. O. Goerbig, Phys. Rev. B **80**, 153412 (2009).

[63] R. de Gail, J.-N. Fuchs, M. Goerbig, F. Piéchon, and G. Montambaux, Phys. B: Condens. Matter **407**, 1948 (2012), Proceedings of the International Workshop on Electronic Crystals (ECRYS-2011).

[64] G. Montambaux, F. Piéchon, J.-N. Fuchs, and M. Goerbig, Eur. Phys. J. B **72**, 509 (2009).

[65] T. Mizoguchi and M. Udagawa, Phys. Rev. B **99**, 235118 (2019).

[66] F. C. de Lima, G. J. Ferreira, and R. H. Miwa, Phys. Chem. Chem. Phys. **21**, 22344 (2019).

[67] C. Si, Z. Sun, and F. Liu, Nanoscale **8**, 3207 (2016).

[68] W. P. Lima, F. R. V. Araújo, D. R. da Costa, S. H. R. Sena, and J. Pereira, Braz. J. Phys. **52**, 1 (2022).

[69] N. W. Ascroft and N. D. Mermim, *Solid State Physics* (Holt-Saunders, Philadelphia, PA, 1976).

[70] M. R. Slot, S. N. Kempkes, E. J. Knol, W. M. J. Van Weerdenburg, J. J. Van Den Broeke, D. Wegner, D. Vanmaekelbergh, A. A. Khajetoorians, C. Morais Smith, and I. Swart, Phys. Rev. X **9**, 011009 (2019).

[71] T. S. Gardenier, J. J. Van Den Broeke, J. R. Moes, I. Swart, C. Delerue, M. R. Slot, C. M. Smith, and D. Vanmaekelbergh, ACS Nano **14**, 13638 (2020).

[72] J. J. van den Broeke, I. Swart, C. M. Smith, and D. Vanmaekelbergh, Phys. Rev. Mater. **5**, 116001 (2021).